Rinke, A., Segger, B., Crewell, S., Maturilli, M., Naakka, T., Nygård, T., Vihma, T., Alshawaf, F., Dick, G., Wickert, J., Keller, J. (2019): Trends of Vertically Integrated Water Vapor over the Arctic during 1979–2016: Consistent Moistening All Over? - *Journal of Climate*, *32*, 18, pp. 6097—6116.

DOI: http://doi.org/10.1175/JCLI-D-19-0092.1

Trends of Vertically Integrated Water Vapor over the Arctic during 1979–2016: Consistent Moistening All Over?

A. RINKE,[a] B. SEGGER,[a] S. CREWELL,[b] M. MATURILLI,[a] T. NAAKKA,[c] T. NYGÅRD,[c] T. VIHMA,[c] F. ALSHAWAF,[d] G. DICK,[d] J. WICKERT,[d,e] AND J. KELLER[f,g]

[a] *Alfred Wegener Institute, Helmholtz Centre for Polar and Marine Research, Potsdam, Germany*
[b] *Institute for Geophysics and Meteorology, University of Cologne, Cologne, Germany*
[c] *Finnish Meteorological Institute, Helsinki, Finland*
[d] *German Research Centre for Geosciences (GFZ), Potsdam, Germany*
[e] *Technische Universität, Berlin, Germany*
[f] *Hans-Ertel-Centre for Weather Research, Climate Monitoring and Diagnostics, Offenbach, Germany*
[g] *German Meteorological Service (DWD), Offenbach, Germany*

(Manuscript received 1 February 2019, in final form 16 May 2019)

ABSTRACT

Arctic trends of integrated water vapor were analyzed based on four reanalyses and radiosonde data over 1979–2016. Averaged over the region north of 70°N, the Arctic experiences a robust moistening trend that is smallest in March (0.07 ± 0.06 mm decade^{-1}) and largest in August (0.33 ± 0.18 mm decade^{-1}), according to the reanalyses' median and over the 38 years. While the absolute trends are largest in summer, the relative ones are largest in winter. Superimposed on the trend is a pronounced interannual variability. Analyzing overlapping 30-yr subsets of the entire period, the maximum trend has shifted toward autumn (September–October), which is related to an accelerated trend over the Barents and Kara Seas. The spatial trend patterns suggest that the Arctic has become wetter overall, but the trends and their statistical significance vary depending on the region and season, and drying even occurs over a few regions. Although the reanalyses are consistent in their spatiotemporal trend patterns, they substantially disagree on the trend magnitudes. The summer and the Nordic and Barents Seas, the central Arctic Ocean, and north-central Siberia are the season and regions of greatest differences among the reanalyses. We discussed various factors that contribute to the differences, in particular, varying sea level pressure trends, which lead to regional differences in moisture transport, evaporation trends, and differences in data assimilation. The trends from the reanalyses show a close agreement with the radiosonde data in terms of spatiotemporal patterns. However, the scarce and nonuniform distribution of the stations hampers the assessment of central Arctic trends.

1. Introduction

Arctic climate change, depicted by a warmer and wetter atmosphere [IPCC 2013; Vihma et al. 2016; Arctic Monitoring and Assessment Programme (AMAP) 2017], is characterized by its amplification compared to the global mean change. Among other amplification factors, such as the poleward energy transports, snow/ice–albedo and cloud–radiation feedbacks, the water vapor–radiation feedback is important (Francis et al. 2009; Serreze and Barry 2011; Wendisch et al. 2017). The amount of water vapor increases with warming following the Clausius–Clapeyron scaling (O'Gorman and Muller 2010). This amplifies the greenhouse effect as increasing water vapor leads to an increase in the downward longwave radiation and affects cloud formation and thus the cloud radiative effect, which subsequently amplifies the near-surface air temperature. The strength of this positive feedback depends on both the sensitivity of the downward longwave radiation to changes in water vapor and the trend in water vapor (e.g., Ghatak and Miller 2013). Atmospheric water vapor in the Arctic increases further because of increased evaporation over ocean regions that are becoming ice free

Denotes content that is immediately available upon publication as open access.

Supplemental information related to this paper is available at the Journals Online website: https://doi.org/10.1175/JCLI-D-19-0092.s1.

Corresponding author: Annette Rinke, annette.rinke@awi.de

DOI: 10.1175/JCLI-D-19-0092.1

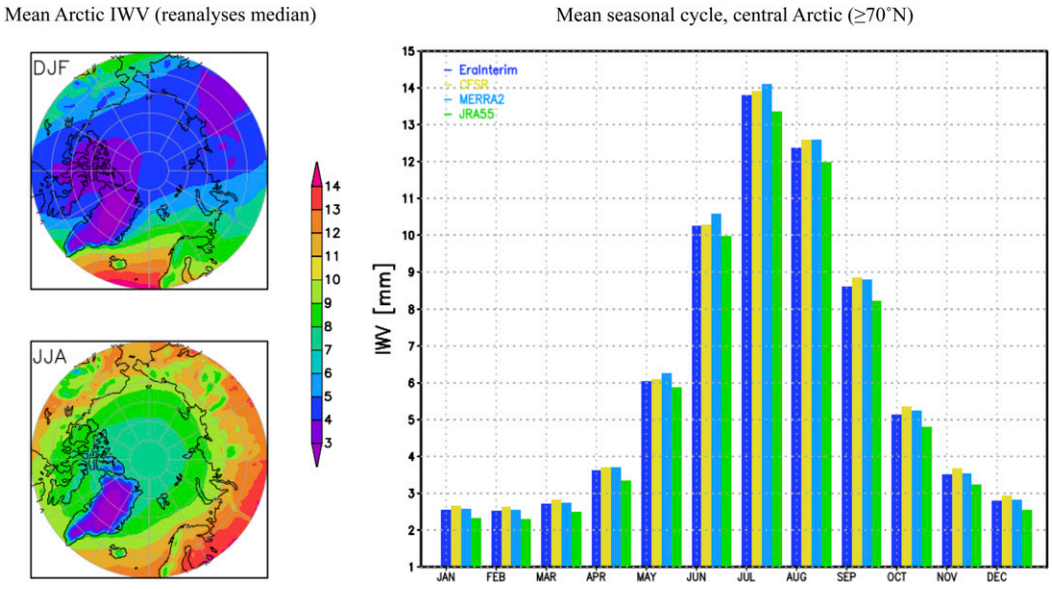

FIG. 1. (left) Spatial maps of (top) winter (DJF) and (bottom) summer (JJA) mean IWV (median of the four reanalyses: CFSR, ERAI, JRA-55, MERRA2) and (right) mean annual cycle of IWV for all four reanalyses. Both plots show the mean IWV (mm) averaged over 1979–2016.

(e.g., Screen and Simmonds 2010; Bintanja and Selten 2014; Boisvert et al. 2015; Kopec et al. 2016). Furthermore, an enhanced moisture transport from lower latitudes into the Arctic has been reported (e.g., Zhang et al. 2012; Woods and Caballero 2016), but this does not have a simple link with enhanced Arctic precipitation (Gimeno-Sotelo et al. 2018). Dufour et al. (2016) did not find an increased meridional moisture transport even though vertically integrated water vapor has increased. Given the importance of Arctic water vapor changes, their investigation based on available long-term climate data is relevant. Here we focus on the change in moisture content in the atmospheric column, that is, the vertically integrated water vapor (IWV). It is well known that the climatological mean IWV over the Arctic is characterized by a pronounced seasonal cycle, with the minimum in winter and maximum in summer (Fig. 1). The different reanalyses agree quite well on the magnitudes, with cross-reanalysis monthly differences being largest (13%–14%) in July and winter months and smallest (5%–6%) in the transition months of May and October, with respect to the mean.

Over the terrestrial Arctic, a few stations provide long-term observations of relative humidity profiles obtained by radiosondes from which IWV can be obtained. In addition to the usual radiosonde biases (see below), the profiles are, however, subject to uncertainties at cold temperatures (Miloshevich et al. 2001). Water vapor products from satellite observations are indirect and subject to large uncertainties, in particular over the Arctic. They are either hampered by clouds (infrared, visible), require sunlight (visible, near-infrared), or are restricted to an underlying surface, that is, open water for microwave imagers or sea ice for microwave sounders. Many satellite-based IWV products have recently become available, but no reference satellite dataset with full coverage of the Arctic exists yet. Schröder et al. (2018) presented the GEWEX Water Vapor Assessment (G-VAP) of IWV products from satellites. The short period of 2003–08 was identified as the maximum common period covered by 22 satellite data records. Their intercomparison showed that the largest relative standard deviations (>25%) are found in polar and high-mountain regions.

Atmospheric reanalyses likely constitute the most comprehensive source of information on the Arctic hydrological budget at present [e.g., Cullather et al. 2000; Lewis et al. 2000; Serreze et al. 2006; Jakobson and Vihma 2010; Cullather and Bosilovich 2011; Dufour et al. 2016; for an overview, see Vihma et al. (2016)]. Reanalyses benefit from assimilation of in situ and remote sensing observations in a manner consistent with model physics and provide long-term gridded datasets with physical interpolation into data-void regions (Thorne and Vose 2010; Parker 2016). In contrast to forecast variables (e.g., precipitation), which are computed based on model physics in the first-guess estimate, atmospheric humidity is an analyzed variable. It is determined via data assimilation and modeling, which integrates all available observations every 6–12 h over the period being analyzed. Such variables are more

consistent among different reanalyses products, compared to forecast variables that rely on model physics (Trenberth et al. 2011). For example, for the Arctic, the cross-reanalysis difference in moisture transport has been estimated to be below 10% (Jakobson and Vihma 2010; Cullather and Bosilovich 2011; Dufour et al. 2016), while that in precipitation can differ by more than 50% (Boisvert et al. 2018). The latter is also because precipitation is the result of a complex chain of processes with many factors' influences and with high spatiotemporal variability, while IWV has much smoother variations with autocorrelation time related to synoptic disturbances (Steinke et al. 2015).

Our investigation builds upon previous studies evaluating the IWV trend in the circumpolar Arctic in reanalyses (Rinke et al. 2009; Serreze et al. 2012; Dufour et al. 2016; Oshima and Yamazaki 2017). While, they pointed to the overall positive Arctic IWV trend, they also highlighted the heterogeneous spatiotemporal patterns of the trend. Indeed, the quantification of the cross-reanalysis differences needs more attention. Therefore, the main aim of our study is a comprehensive intercomparison of the circum-Arctic IWV trend across four different reanalysis datasets, including their evaluation against station observations. Our focus is to present what we know (in)consistently about the Arctic IWV trends taking into account the high spatiotemporal variability.

We extend the previous studies by various important aspects: (i) We analyze four modern global reanalyses and include the recent period covering 1979–2016. (ii) As annual means and averages over the whole Arctic might mask regional and seasonal details, we present monthly spatial trends to highlight important differences from month to month and from region to region. (iii) We show the cross-reanalysis range in the monthly IWV trends to quantify their uncertainty and estimate the maximum IWV trend over the last 38 years. (iv) We discuss the interannual IWV variations, which underlie the trend. (v) In concert with the reanalyses, we analyze available circum-Arctic radiosonde data from 36 stations north of 65°N. Further, we include selected IWV data from tropospheric products from processing global positioning system (GPS) data.

2. Data and analysis

a. Reanalyses

We evaluate four modern global atmospheric reanalyses, namely, the National Centers for Environmental Prediction (NCEP) Climate Forecast System Reanalysis (CFSR; Saha et al. 2010, 2014), the European Centre for Medium-Range Weather Forecasts (ECMWF) interim reanalysis (ERA-Interim, hereafter ERAI; Dee et al. 2011), the Japanese Meteorological Agency (JMA) 55-year Reanalysis (JRA-55; Kobayashi et al. 2015), and the NASA Global Modeling and Assimilation Office (GMAO) Modern-Era Retrospective Analysis for Research and Applications, version 2 (MERRA2; Gelaro et al. 2017).

We restrict our analysis to these four reanalyses because they cover the period since the beginning of the satellite era at a relatively high spatial resolution (Table 1) and they are "full input" reanalyses (Fujiwara et al. 2017), that is, systems that assimilate surface and upper-air conventional and satellite observation data, in contrast to "surface input" reanalyses. We do not include precursor reanalyses from JMA, NASA, and NCEP that have coarser resolutions and older models behind them, or the next-generation ECMWF reanalysis, ERA5, as it was not available when we started the analysis.

The reanalyses differ in their horizontal and vertical resolution, physical parameterizations, and assimilation scheme and input data. Fujiwara et al. (2017) provide all the details about this, such as horizontal and vertical grids, execution streams, assimilated data (their Tables 1 and 2, their Figs. 6 and 8–10, and their supplemental tables), and major physical parameterizations in the reanalysis forecast models (their Table 3). Table 1 summarizes the main relevant characteristics of the four global reanalyses used in our study. In terms of assimilated data, we focus on those measurements that are most directly related to moisture. See the given references and Fig. S1 in the online supplemental material for more details. Differences in the reanalyses' representations of sea ice (Table 1) may contribute to differences in air humidity at low altitudes. Fujiwara et al. (2017) provide the detailed sources of sea surface temperature (SST) and sea ice lower boundary conditions used in the different reanalyses (their Table 4).

All reanalyses assimilate humidity-related data and also atmospheric motion vectors, which might improve the representation of moisture advection. However, it should be mentioned that because of the challenging conditions in the central Arctic (north of 70°N), very few measurements are assimilated and differences between different reanalyses might arise even from the rejection of individual observations within the different quality-control schemes. Table 1 gives detailed information about humidity-relevant data assimilation. Note that microwave imager radiance data around the 22-GHz water vapor line, for example, SSM/I and AMSR, which are strongly related to IWV even under cloudy conditions, are only assimilated over open water surfaces. The assimilation of radiances measured by microwave sounders, for example,

TABLE 1. Characteristics of the four global atmospheric reanalyses used in in our study. Note that all reanalyses assimilate surface reports from land stations and ships but employ different quality checks. Further data assimilation information can be found in the supplemental material (Fig. S1).

	CFSR	ERAI	JRA-55	MERRA2
Horizontal resolution	CFSR: T382 (~38 km), CFSv2: T574 (~27 km)	T255 (~79 km)	T319 (~55 km)	0.5 lat × 0.625 lon (~55 km)
Vertical levels	64	60	60	72
Sea surface temperature and sea ice	Coupled to GFDL MOM	Multiple datasets (NOAA, ECMWF)	COBE-SST	Multiple datasets (NOAA)
Convection parameterization scheme	Modified Tiedtke (shallow), simplified Arakawa–Schubert with momentum mixing (deep)	Jakob and Siebesma (shallow), Fritsch–Chappell (deep)	Prognostic Arakawa–Schubert with downward CAPE	Relaxed Arakawa–Schubert (shallow) with Tokioka-type trigger (deep)
Assimilation scheme	3D-Var	4D-Var	4D-Var	3D-Var
Humidity assimilation	Yes	Yes	Yes	Yes
Radiosondes humidity assimilation	Yes	Yes, but excluded in extremely cold conditions	Yes	Yes
Satellite radiances	AMSU-B, HIRS, MHS, SSM/I (S)	HIRS, AMSU-B, MHS	AMSU-B, HIRS, MHS, VTPR, AMSR-E, AMSR-2, SSM/I (S), TMI	AMSU-B, HIRS, MHS, VTPR, SSM/I(S)
Infrared spectrometer	AIRS (since 2008), IASI (since 2008)	AIRS (since 2004)	—	AIRS (since 2002), IASI (since 2008) only clear sky
Microwave imager retrieval	AMSR-E (only surface quantities)	Partly SSM/I IWV	—	SSM/I, TMI rain rates
Radio occultation	Since 2001	Since 2001	Since 2006	Since 2004
Reference	Saha et al. (2010, 2014)	Dee et al. (2011)	Kobayashi et al. (2015)	Gelaro et al. (2017)

AMSU-B and the Microwave Humidity Sounder (MHS), making use of the stronger 183-GHz line, is limited to channels with high opacity to avoid surface contamination and can therefore only represent higher vertical levels. At the higher microwave frequencies, liquid clouds emit strongly, and the presence of clouds with larger ice water content can further limit their assimilation. Several of the instruments have been on board different satellites, and as sensor intercalibration is an ongoing research item, break points due to changes in the satellite constellation can occur. Similarly, the event of global navigation satellite system (GNSS) radio occultation measurements of the bending angle being sensitive to temperature and moisture led to the assimilation of roughly 2000 profiles per day since the mid-2000s. More details about satellite data assimilation can be found in Fig. S1 in the online supplemental material.

b. Station data

We analyze IWV derived from specific humidity profiles based on the relative humidity observed by radiosondes launched at Arctic land stations. From the Integrated Global Radiosonde Archive (IGRA; Durre et al. 2006), we use IWV data of 36 stations in the Arctic north of 65°N (Fig. 2), following Naakka et al. (2018). The archive contains data from the individual beginning of radiosonde measurements at each station, so within the analyzed period, the availability of data from the stations varies. The soundings were mostly taken twice per day (at 0000 and 1200 UTC) but on some stations once daily only (e.g., in Ny-Ålesund, Norway, at 1200 UTC). As missing data due to technical or quality-related problems of soundings occur throughout the whole period, we apply a threshold to calculate a monthly mean. We choose to require at least 85% data coverage for a representative monthly mean value, that is, we require at least 26 sounding days for months with 30 or 31 days and at least 24 sounding days for February in non–leap years.

Obviously, the IGRA has the advantage to contain an extensive collection of worldwide available radiosonde data that have undergone a formal quality control regarding, for example, formatting problems and physically implausible values (Durre et al. 2006). In addition to the data value repetition check for dewpoint depression, implausible humidity values are removed if the reported dewpoint depression is out of the range of 0°–70°C (Durre et al. 2006, see their Table 4).

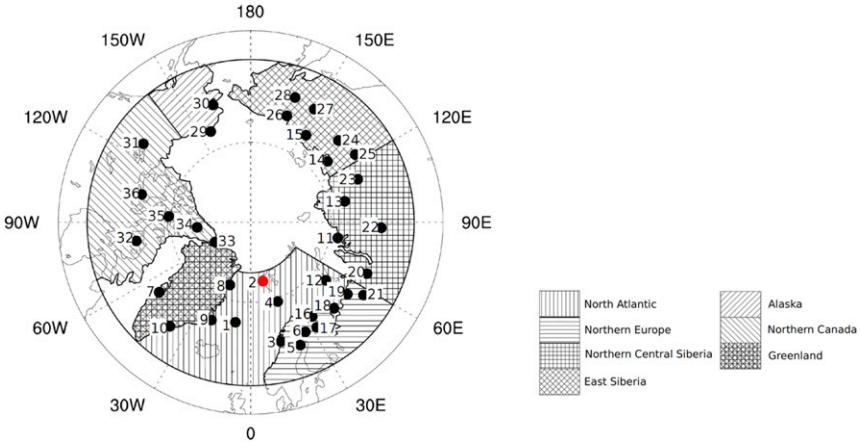

FIG. 2. Study region and the location of the 36 radiosonde stations in seven subregions (Nordic and Barents Seas, northern Europe, north-central Siberia, east Siberia, northern Canada, Alaska, and Greenland). The regions include the following sounding stations: Nordic and Barents Seas: Jan Mayen (1), Ny Ålesund (2), Bodo (3), Bear Island (4), and Malye Karmakuly (12); northern Europe: Luleå Kallax (5), Sodankylä (6), Murmansk (16), Kandalaksa (17), Shoina (18), Narian Mar (19), and Pechora (21); northern central Siberia: 11 Ostrov Dikson, 13 Khatanga, 20 Sale-Khard, 22 Turuhansk, 23 Olenek; east Siberia: Tiksi (14), Cokurdah (15), Verkhoyansk (24), Gigansk (25), Cherskiy (26), Zyrianka (27), and Omolon (28); northern Canada: Norman Wells (31), Hall Beach (32), Alert (33), Eureka (34), Resolute Bay (35), and Cambridge Bay (36); Alaska: Barrow (29) and Kotzebue (30); Greenland: Egedesminde (7), Danmarkshavn (8), Scoresbysund (9), and Ammassalink (10). The supersite Ny-Ålesund (78.9°N, 11.9°E) is marked in red.

Yet, the general inhomogeneity of used radiosonde sensor types across the different stations, and even the temporal inhomogeneity throughout a single station's data record over time, may hinder retrieving long-term climate trends (Elliott and Gaffen 1991; Moradi et al. 2013).

Recognizing this shortcoming of the vast operational dataset for the potential use in climate studies, the Global Climate Observing System (GCOS) Reference Upper-Air Network (GRUAN) has been implemented (Seidel et al. 2009; Bodeker et al. 2016). Within GRUAN, a small set of observational sites make an effort to assure high-quality reference observations from different sensors. In the Arctic region north of 65°N, the three sites Ny-Ålesund; Sodankylä, Finland; and Barrow, Alaska (now known as Utqiaġvik), contribute with their radiosonde measurements. The resulting GRUAN radiosonde data are centrally processed with manufacturer-independent corrections accounting for, for example, the radiation dry bias and time lag in humidity measurements, and quantified measurement uncertainties are provided (Dirksen et al. 2014). Unfortunately, the GRUAN radiosonde data (Sommer et al. 2012) are only available for a short period (since 2011) at all three Arctic stations. However, the Ny-Ålesund radiosonde record prior to the GRUAN period has been homogenized, accounting for various sensor-related corrections in the earlier radiosonde types (Maturilli and Kayser 2017a). We use this homogenized Ny-Ålesund (NYA) radiosonde record from 1994 to 2016 (Maturilli and Kayser 2016, 2017b), which we call in the following homogenized NYA, as high-quality long-term station observation for comparison with the reanalyses and the other observations (IGRA, GPS).

Ground-based GPS zenith path delay measurements are an established tool for IWV observation (Bevis et al. 1992; Wang et al. 2007; Ning et al. 2016a). These data provide an independent IWV dataset because they are so far not assimilated into the reanalyses. Although the GPS-based wet delay is converted into water vapor using the atmospheric weighted mean temperature that is calculated using reanalysis data, the quality of the IWV products does not change compared to using radiosonde temperature measurements (Ning et al. 2016b). We inspected a subset of GPS observations north of 65°N (Deng et al. 2016; Alshawaf et al. 2018), which covers 35 sites (Fig. S2). It becomes obvious that these GPS station locations have almost no overlap with the radiosonde stations. From the GRUAN stations, only Ny-Ålesund is collocated with a GPS station from this subset. The GPS stations are clearly focused on the Greenland coast and only three stations are in Russia. Furthermore, the temporal coverage is short; most observations start in the mid-2000s. Therefore, a comparison with the complete

IGRA data is not feasible, but we limit it to the supersite Ny-Ålesund (Fig. 2).

c. Analysis methods

Our study of the reanalyses trends is focused on monthly IWV data for the 38-yr period 1979–2016. For the intercomparison, the reanalyses have been remapped onto the 0.75° × 0.75° latitude–longitude grid of ERAI, using bilinear interpolation. The presented spatial plots from reanalyses for the Arctic region show the domain north of 60°N (Fig. 2). We define the region north of 70°N as the central Arctic and present accordingly area-weighted averaged values. Because there are distinct variations within a season, we analyze the IWV trends for each month.

Linear trends have been calculated by linear least squares regression, with statistical significance assessed by a bootstrapping approach (Kiktev et al. 2003). At each grid point, a series of actual data points ($N = 38$) is decomposed into a linear trend and a time series of trend residuals or "noise." The bootstrap technique randomly selects N values from the residuals to form a time series of residual variations of same length N. The residuals are resampled 1000 times to generate sets of plausible noise sequences. Afterward, each noise is added back onto the best-fit line from the original trend analysis, and the trend is reestimated. The finally produced distribution of 1000 trends is used to determine the significance: The trend at each grid point is statistically significant at the 95% level if a zero trend falls within either the upper or lower 2.5% tail of its bootstrapped distribution.

For the comparison between the reanalyses and the observational data, the station-nearest land grid point from the reanalyses has been selected. An examination of the four surrounding grid points showed that the results are solid, that is, not sensitive to the choice of either grid point. The monthly means of the reanalyses have been calculated based on the same temporal data coverage as given by the available station data. This was done to ensure that the reanalyses were comparable to in situ data and not to improve the trend estimate. Therefore, these trends can differ from the reanalysis trends based on full 6-hourly × 38-yr coverage. We group the IGRA station data to seven subregions (Nordic and Barents Seas, northern Europe, northern central Siberia, east Siberia, northern Canada, Alaska, and Greenland; Fig. 2) and calculate the average of the stations for each subregion. The regions have been basically selected based on the spatial patterns of specific humidity conditions in the lower troposphere (Naakka et al. 2018). We further present an all-station (Arctic) average. Finally, according to the above described data availability, we use the Ny-Ålesund observations from the different sources (IGRA, NYA, GPS) for 1994–2016 to compare with reanalyses and check the data consistency.

3. Long-term Arctic IWV trends in reanalyses

a. Spatiotemporal patterns of trend

Although the intercomparison of the monthly IWV trends for 1979–2016 (Fig. 3) suggests an agreement of the reanalyses that the Arctic has become wetter in almost all regions, we cannot confirm this because of the statistical insignificance of most trends. Indeed, we find consistently across all reanalyses significant IWV trends only over specific regions for specific months.

1) AGREEMENT

Significant positive trends occur consistently in all reanalyses (Fig. 3):

(i) A positive trend occurs over the Atlantic sector of the Arctic, specifically over the Nordic and Barents Seas from summer to winter (August–January), over the Barents and Kara Seas in May and November–February, and over Scandinavia in summer (July–September) and early winter (November–December). The IWV increase over the Atlantic sector of the Arctic has been discussed by many studies (e.g., Serreze et al. 2011, 2012; Stroeve et al. 2012; Boisvert et al. 2015; Woods and Caballero 2016; Dufour et al. 2016) being related to a set of factors, including increasing temperature and moisture advection (Fig. S3), increasing sea surface temperature, and reduced sea ice extent in recent decades. Figure S4a shows exemplarily that the moistening occurs throughout the tropospheric column, but predominantly in low levels (below 850 hPa). This is consistent with a bottom-amplified warming and moistening (e.g., Screen and Simmonds 2010; Woods and Caballero 2016).

(ii) A positive trend occurs over the Canadian archipelago and Baffin Bay in summer (June–August), which is consistent with the negative trend in sea ice concentration over Baffin Bay in June–July. In addition, a mean sea level pressure (SLP) increase over/north of Greenland in summer supports the intrusion of moist, warm air from lower latitudes toward northern Canada (Fig. S3).

(iii) A positive trend occurs over the Chukchi and East Siberian Seas in autumn (September–October), which is related to the strong sea ice retreat and related heat fluxes, increased near-surface temperature and water vapor holding capacity of air (e.g., Serreze et al. 2012). The according moistening is

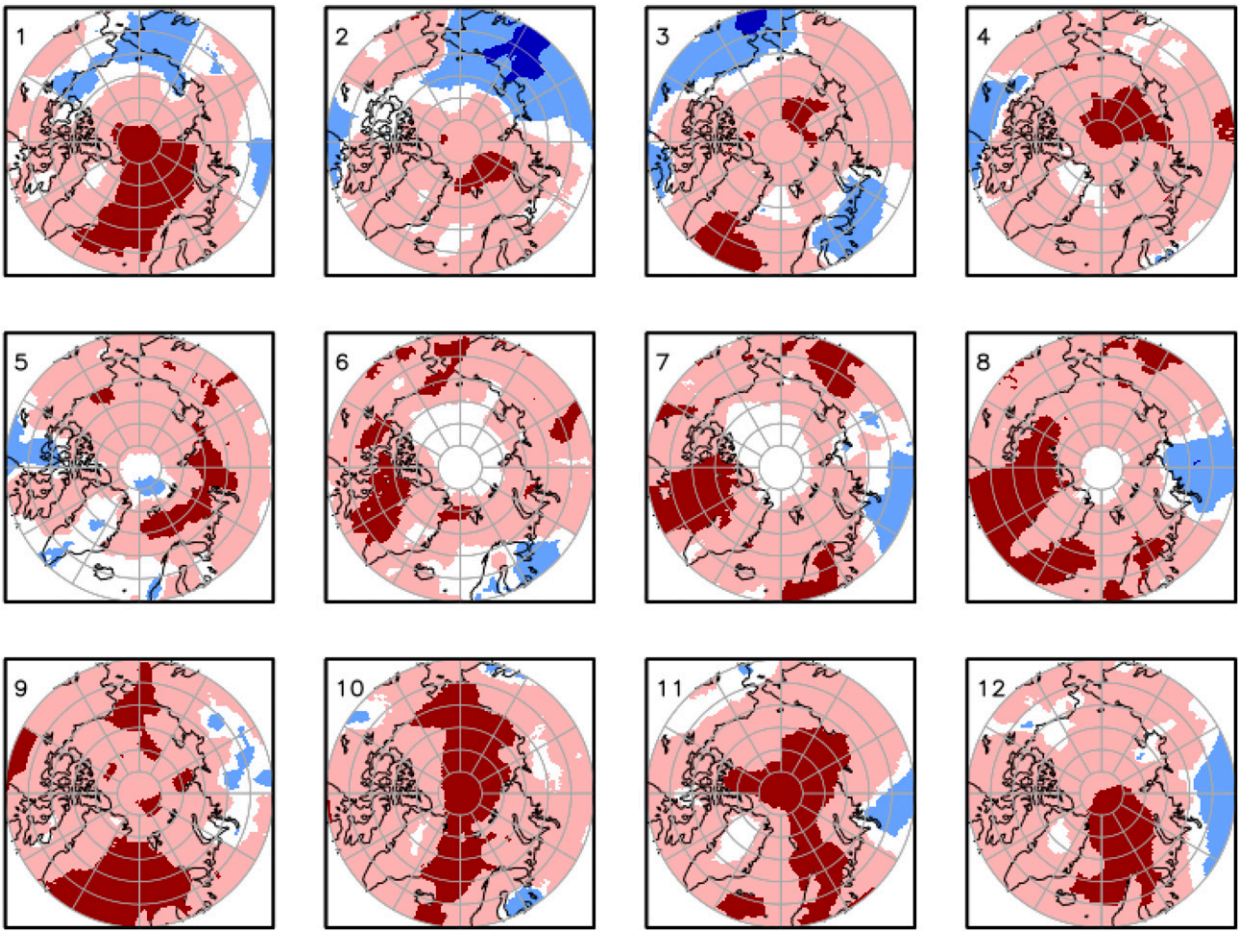

FIG. 3. Agreement in the monthly IWV trends (1 for January, 2 for February, ...) across the four reanalyses (CFSR, ERAI, JRA-55, MERRA2) for 1979–2016. Color shading indicates those areas where all four reanalyses agree on the sign of the trend (red: positive trend; blue: negative trend). White indicates locations where the reanalyses disagree on the sign of the trend (i.e., at least one is different from the others). The dark red (blue) colors mark regions of positive (negative) trends, which are significant at the 95% level in all four reanalyses.

confined to low levels again (Fig. S4b). Moisture advection contributes, particularly in October (Fig. S3).

(iv) A positive trend occurs over other parts of the Siberian Arctic sector, specifically over the northern Laptev Sea in spring (particularly in April) and over east Siberian land region in summer (July–August), which fits with the circulation-driven warm/moist air transport into those regions (Fig. S3).

(v) A positive trend occurs over larger parts of the central Arctic Ocean in autumn–winter (September–January). This is consistent with an increasing moisture transport over the North Atlantic sector into the central Arctic (Fig. S3) related to cyclones/moist intrusion (e.g., Woods and Caballero 2016; Rinke et al. 2017).

Remarkably, a few regions indicate a statistically significant negative IWV trend, consistently in all reanalyses (Fig. 3):

(i) In winter, this trend is shown over eastern Siberia (in February) and the Bering Strait region (in March). This drying is related to atmospheric circulation changes (SLP pattern) and the associated more frequent northerly wind, and thus cooling and drying in that region in winter (Fig. S3). Our result is consistent with findings of Serreze et al. (2012) and Liu et al. (2007). Although the negative moisture trend occurs in the whole troposphere, Fig. S4c shows a clear maximum drying near the 850-hPa level well above the inversion layer common in winter. This level represents the maximum of the specific humidity profile and occurs where the net

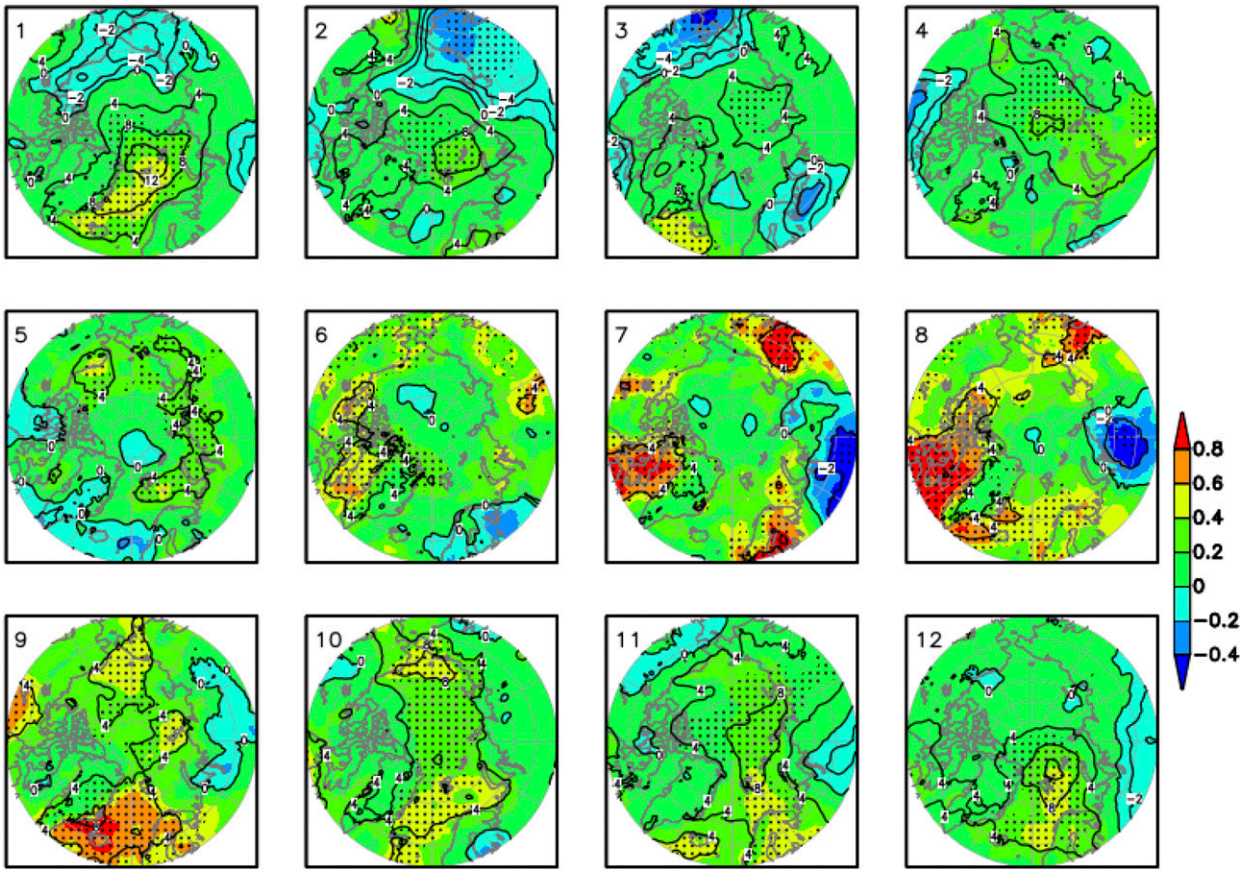

FIG. 4. Monthly IWV trends (mm decade^{-1}; color shading) based on the median of the four reanalyses (CFSR, ERAI, JRA-55, MERRA2) for 1979–2016. Stippling indicates significant trends (at the 95% level). Black isolines show the percentage trend (% decade^{-1}) relative to the climatological monthly mean over all reanalyses.

meridional moisture fluxes are strongest (Serreze et al. 1995).

(ii) In summer (particularly in August), this trend is shown over north-central Siberia, which corresponds with a negative SLP trend over the region of Taymyr Peninsula and the Kara and Laptev Seas and the associated increased transport of cold, dry air from the north into that region (Fig. S3). The drying is prominent over the entire troposphere (Fig. S4d), again reflecting the circulation changes.

In general, changes in meridional moisture transport caused by changes in atmospheric circulation are the reason for many of the regional trends in IWV. Therefore, we highlight this exemplarily for ERAI (Fig. S3).

Figure 4 shows the monthly IWV trend estimate over the Arctic region based on the median of the four reanalyses. We calculate the strongest relative increase (>8% decade^{-1}; with respect to the median) over the Arctic North Atlantic in winter (November–February) and over the Chukchi and East Siberian Seas in autumn (October). With respect to the absolute magnitudes, the largest moistening occurs in summer over north-central Siberia (~1.0 ± 0.5 mm decade^{-1} in June), over the Arctic portion of the North Atlantic (e.g., ~0.9 ± 0.4 mm decade^{-1} in August), over the Canadian archipelago and Baffin Bay (e.g., ~1.1 ± 0.4 mm decade^{-1} in August), and over the east Siberian land (e.g., ~1.1 ± 0.5 mm decade^{-1} in August). The reanalyses agree on the presented spatiotemporal patterns of the trend, with an all-pair-averaged pattern correlation coefficients of 0.9.

2) DISAGREEMENT

The reanalyses substantially disagree on the regional trend magnitudes (Fig. 5). CFSR is the reanalysis that produces the maximum trend (out of all four reanalyses) over the Arctic North Atlantic in all months and over the central Arctic Ocean in the cold season (October–March), whereas ERAI yields the maximum over the Arctic Ocean in the warm season (May–August). Over the

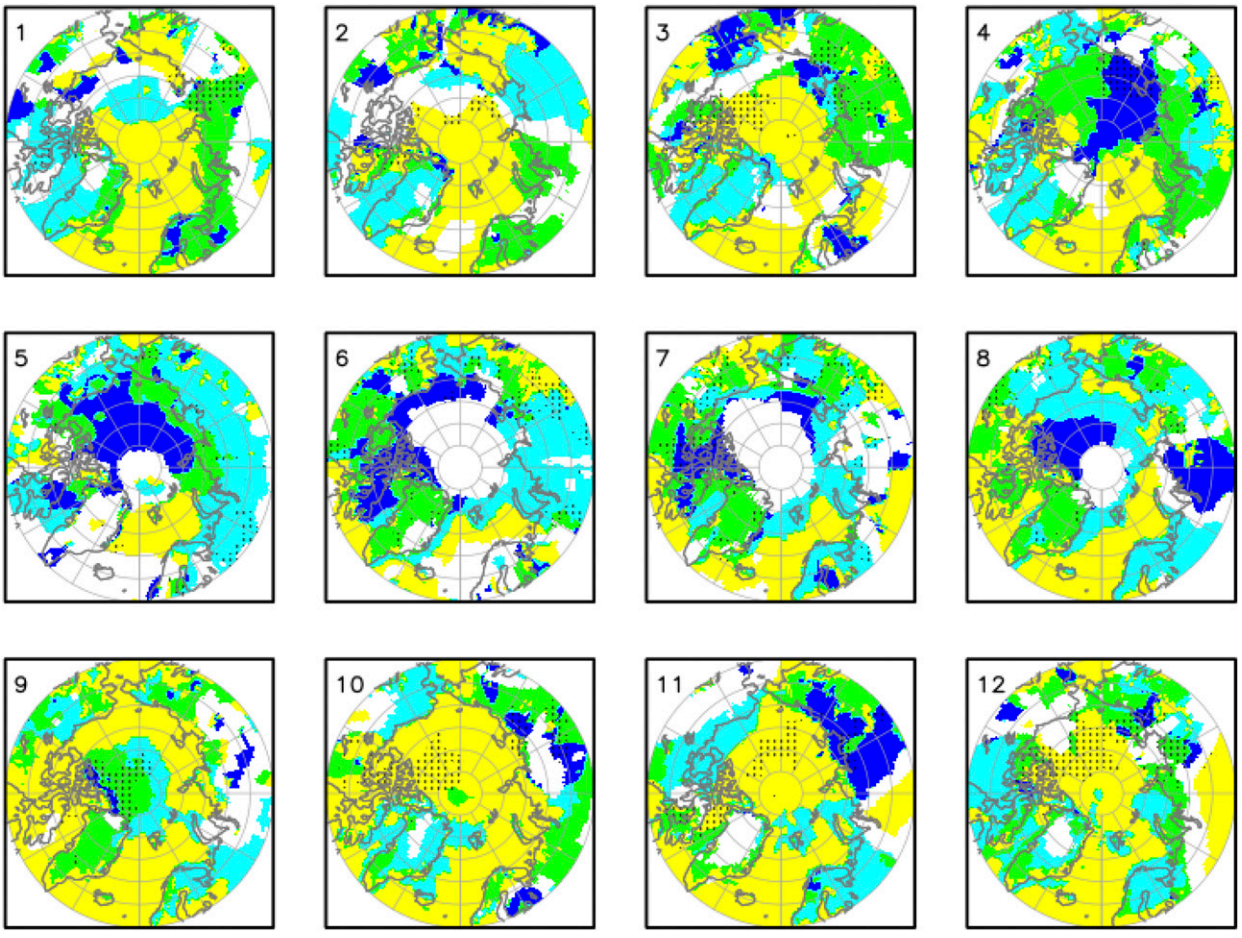

FIG. 5. Reanalysis, which has the maximum (positive or negative) trend out of the four reanalyses at a grid point (CFSR: yellow; ERA-Interim: dark blue; JRA-55: green; MERRA2: light blue), based on the monthly IWV trend for 1979–2016. White indicates where the reanalyses disagree on the sign of the trend (i.e., at least one is different from the others). Stippling indicates where the trend of the reanalysis with the maximum trend is significantly different (at the 95% level) from the trend of the reanalysis with the second largest trend.

Arctic Ocean, CFSR and ERAI are the reanalyses that show the extremes (i.e., maximum or minimum out of all reanalyses). IWV trends and their assignment to the regional minimum trend are the opposite of the maximum trend (Fig. 5 and Fig. S5), respectively. Those reanalyses, which show the maximum and minimum IWV trends, are not completely the same when inspecting the 2-m air temperature trends (not shown) for all regions and months. This stresses that the IWV trend is controlled not only by the temperature trend but also by trends in moisture transport and evaporation [see section 3a(3)].

We quantify the differences in the trend magnitudes across the four reanalyses by the range of the ''maximum minus minimum IWV trend'' for each grid point (Fig. 6). This figure clearly highlights the regions and months of greatest uncertainty among the reanalyses, where the absolute difference is largest, namely, larger than 0.5 mm decade^{-1} (which is equivalent to more than 50%, relative to the reanalyses-mean trend). That appears in the summer season and over the following three regions:

(i) It appears over the central Arctic Ocean in summer (June–August). This is the identified region/season with prominent disagreement across the reanalyses with respect to the IWV trend sign (Fig. 3). The negative trend in CFSR is in contrast to the insignificant or positive trends in the other three reanalyses. Associated with this, CFSR shows a strong negative trend anomaly with respect to the reanalyses' median, while the other reanalyses show positive anomalies (largest in ERAI) (Fig. S6). Actually, we do not expect large anomalies in near-surface specific humidity in summer because of the melting snow or sea ice, which keeps the surface air temperature near 0°C and thus limits the change in the surface saturation vapor pressure.

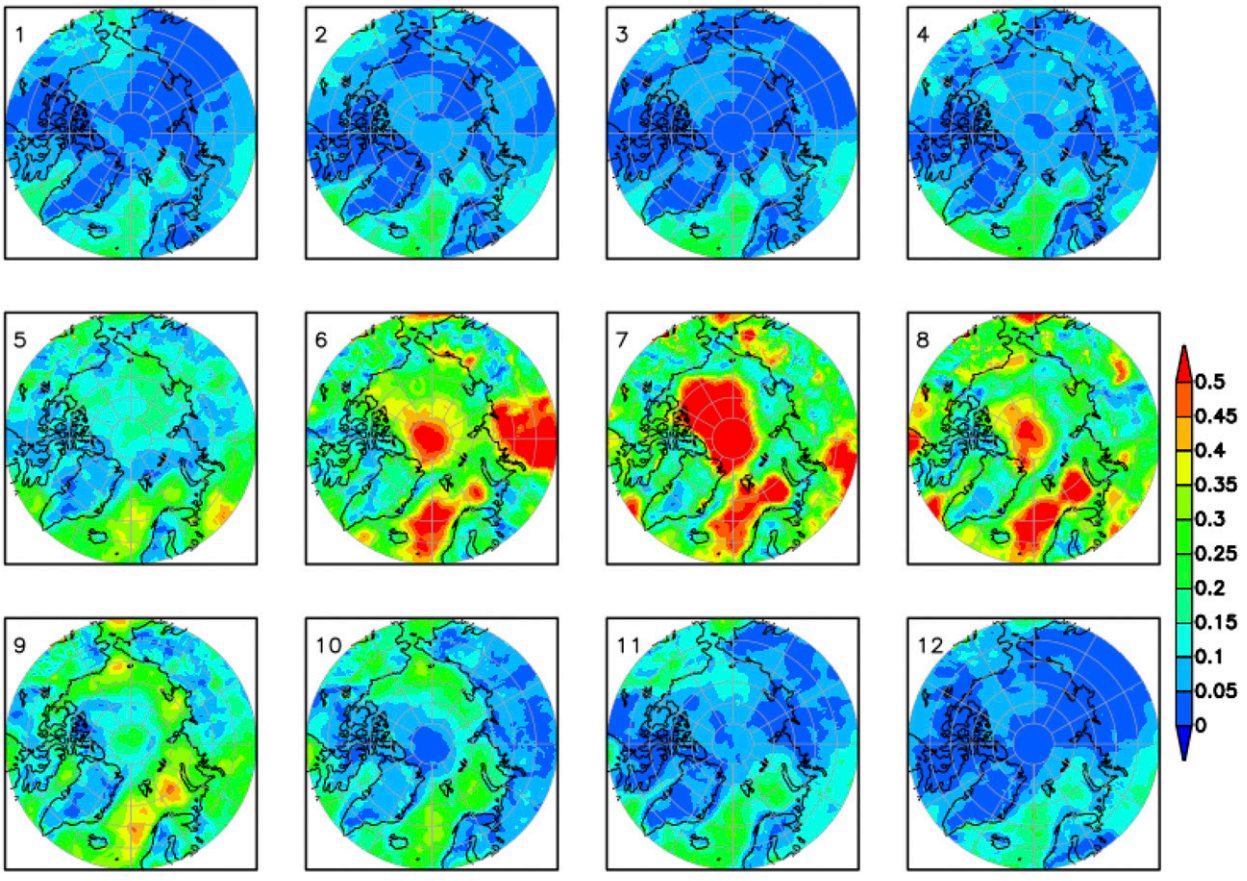

FIG. 6. Range of the monthly IWV trends (mm decade^{-1}) across the four reanalyses (CFSR, ERAI, JRA-55, MERRA2) for 1979–2016. At each grid point, the difference of maximum minus minimum IWV trend is plotted. The maximum and minimum trends are those out of the four reanalyses.

Therefore, Serreze et al. (2012) argued that an IWV trend over the central Arctic Ocean in summer is not expected. However, a change in moisture transport (Fig. S3) may well generate an IWV trend. Accordingly, differences in moist-air advection (Cullather and Bosilovich 2011; Dufour et al. 2016; Naakka et al. 2019), subsequent moist processes in the models behind the reanalyses, as well as differences in data assimilation are potential contributing factors for the presented cross-reanalysis differences.

(ii) It appears over the Arctic portion of the North Atlantic, namely, the Nordic and Barents Seas, in summer (Figs. 3, 6). This cross-reanalysis difference in the IWV trend is due to large positive trend anomalies in CFSR and MERRA2 compared to the median trend (Fig. S6). Both reanalyses show significant positive trends (e.g., 0.7 ± 0.3 mm decade^{-1} in July), while ERAI and JRA-55 indicate insignificant trends. Apparent factors that potentially contribute to those differences among the reanalyses are evaporation trends, which differ for diverse humidity profile, wind and stratification (Boisvert et al. 2015), and different moisture advection changes (Dufour et al. 2016). Sherwood et al. (2014) pointed out that differences in lower-tropospheric vertical mixing might also play a role, which can modify the trend in the specific humidity profile (Fig. S7), for example, by varying vertical thermal stability and wind shear changes. It has been further argued that different vertical mixing can affect moisture advection, such that weaker (stronger) mixing allows (prevents) moist air advection to penetrate farther to the north without strong cooling/drying (Naakka et al. 2018).

(iii) It appears over northern central Siberia in summer. The large cross-reanalysis differences in the IWV trend in this land region in early summer (June; Fig. 6) are caused by MERRA2 being an outlier. This reanalysis shows a large significant positive IWV trend (1.1 ± 0.5 mm decade^{-1}), which the other three reanalyses do not agree with, and leads

to a large positive trend anomaly in MERRA2 compared to the median trend (Fig. S6). Certainly, this is associated with a stronger SLP reduction over the region covering the Ural Mountains and west Siberian plain compared to the other reanalyses, which can trigger a stronger inflow of warm, moist air from the south to northern central Siberia. It is known that cyclones from Siberia are effective in transporting water vapor to the Arctic in summer (e.g., Komatsu et al. 2018), and MERRA2 has been detected as an outlier in the trend of summer cyclone frequency, compared to the other reanalyses (Zahn et al. 2018).

3) Further discussion of cross-reanalysis differences

In general, it is difficult to identify the exact causes for differences in the reanalyses' trend patterns (Chung et al. 2013; Lindsay et al. 2014; Boisvert et al. 2018) as they may arise from various sources. However, we provide some possible reasons for these differences in the following.

In the previous section, we quantified the largest cross-reanalysis differences in the IWV trend that occur in summer over three specific regions. We identified those reanalyses that are the responsible outliers, and then discussed the related physical mechanisms behind them. Here, we provide further discussion of these factors. The identified regions (Fig. 6) appear neither in the near-surface temperature (Fig. S8) nor in the evaporation (Fig. S9) trend differences but emerge in the 850-hPa relative and specific humidity trend difference (Fig. S9). This is an indication of the importance of moisture transport for IWV trend differences in those regions in summer.

Differences in atmospheric circulation strongly affect the transport of warm/moist air from the south into the Arctic or transport of cold/dry air from the central Arctic southward. The cross-reanalysis difference in SLP trend is 1–2 hPa decade^{-1} (Fig. S8) and of the same magnitude as the SLP trend in an individual reanalysis. Hence, the differences in SLP trend and their uneven spatial distribution can cause notable differences in the trends of the horizontal moisture transport, and they control the distribution of moisture transport to different regions. Trends in the moisture transport are on the order of 10 kg (m s^{-1})$^{-1}$ decade^{-1} (Fig. S3), which is about 10% of the mean transport.

Differences in IWV trend are further related to differences in air temperature and evaporation. The cross-reanalysis differences in the near-surface air temperature trend are relatively small (0.5°–1.5°C decade^{-1}; Fig. S8). Larger differences occur during the cold seasons along the coastline and sea ice edge because of different model resolution and sea ice handling (see section 2a). This is apparent in the cross-reanalysis differences in the sea ice concentration trend, which is more than 10% decade^{-1} near the ice edge (Fig. S8). These sea ice differences are reflected in the evaporation trend differences (Fig. S9). Absolute differences of 0.2–0.4 mm day^{-1} decade^{-1}, as occurred in the Barents and Kara Seas in the cold season and in the Chukchi Sea in late autumn (October–November), represent large relative differences of up to 100%, relative to the reanalyses' median evaporation trend. This indicates that evaporation differences among the reanalyses contribute to those in IWV there.

Another source of the discussed deviations between the IWV trends in the reanalyses is the representation of the physical processes, specifically of moist processes, in the models. For instance, while all four reanalysis systems use a parameterization for deep and shallow convection, the implementations or even approaches differ (Table 1; section 2a), which leads to differences in the representation or distribution of moisture in the atmosphere. Further, with respect to the lower boundary conditions, different land models are used in the four reanalysis systems, influencing the exchange of heat, moisture, and energy between the atmosphere and Earth's surface. Also, for the ocean, the representation of SST and sea ice varies among the reanalyses (Table 1; section 2a) with the potential to produce significant deviations among the four datasets (see above).

Another contribution to the differences across the reanalyses is the application of various data assimilation approaches and implementations (Table 1; Fig. S1; section 2a). Although all reanalyses assimilate more or less the same available radiosonde sounding and surface data (albeit employing different quality checks), a source for variations of trends in IWV among the different reanalyses is the assimilation of satellite data. Figure S10 shows the analysis increments in water vapor for ERAI for the lowest 35 model levels averaged over the central Arctic. It can clearly be seen that, besides the model bias, trends and even jumps in the analysis increments happen over time for the various seasons, especially summer. These changes originate from the changing observing system or, more specifically, from new satellite data assimilated into the model state (e.g., Fujiwara et al. 2017). A similar behavior is known for other reanalyses and the characteristics, and the extent of these artificial trends and jumps highly depends on the specific implementation of the data assimilation for each satellite as well as its bias correction. In addition, not all reanalyses use the same satellite observations or same periods for each of

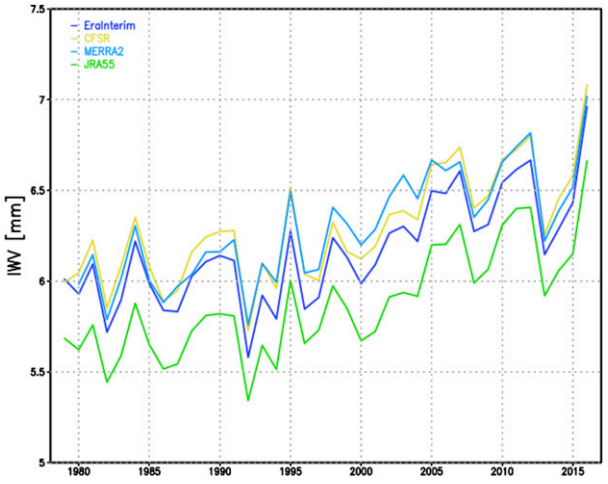

FIG. 7. Annual IWV (mm) time series for the central Arctic (≥70°N) for the four reanalyses (CFSR, ERAI, JRA-55, MERRA2) for 1979–2016.

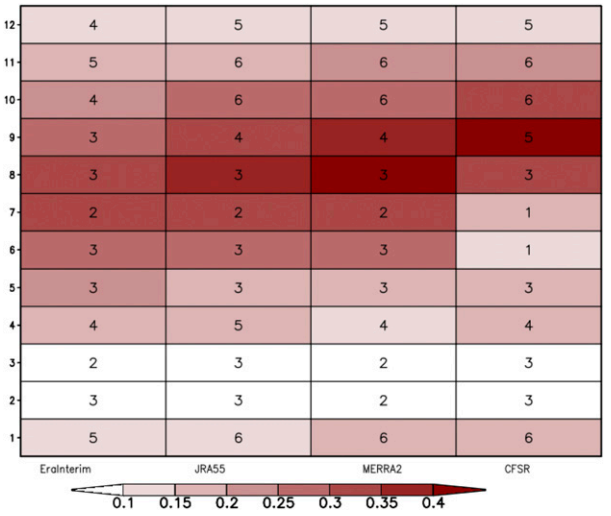

FIG. 8. Monthly IWV trend for the central Arctic (≥70°N) for the four reanalyses (CFSR, ERAI, JRA-55, MERRA2) for 1979–2016. The *x* axis indicates the individual reanalysis and the *y* axis indicates the 12 months. All trends are significant at the 95% level, except during February. The color shows the absolute trend (mm decade^{-1}), while the numbers are the percentage trend (% decade^{-1}), relative to the climatological monthly mean of each reanalysis.

these observing systems (see section 2a; Table 1, Fig. S1). Therefore, the treatment of satellite data in the reanalysis production process is a major contribution to the variations of IWV trends among the different reanalyses. It is ultimately complicated to distinguish the true effects of aforementioned differences in the data assimilation procedures and the moisture transport, as the latter is calculated from the gradients and winds that are also already (more or less) affected by data assimilation.

Without the possibility of running identical-twin experiments on the reanalysis systems, it is not possible to distinguish between the various aforementioned effects on the differences in the representation of IWV trends over the Arctic. We therefore expect the disagreements among the four datasets to be the combined result of most or all of these effects.

b. Trends and variability in the central Arctic

Here we present results for the central Arctic IWV, that is, area-weighted average over the polar cap north of 70°N. Despite the disagreement on the yearly magnitude of IWV (JRA-55 being the driest, showing values ~0.5 mm smaller than the wettest reanalyses—CFSR and MERRA2), the reanalyses agree on an increase of the central Arctic IWV over 1979–2016 (Fig. 7). The figure indicates a relatively small increase during the first two decades and a distinct increase started sometime around year 2000. The Arctic IWV further shows a pronounced interannual variability. The monthly IWV trends are provided in Fig. 8. Consistently across all reanalyses, the trends are significant (at the 95% level) and positive in all months (except in February), with the highest absolute trend in summer (>0.3 mm decade^{-1}) and lowest one in winter (<0.2 mm decade^{-1}). The lowest trend (<0.1 mm decade^{-1}) occurs specifically in February–March, which is again a common feature in the reanalyses. According to the reanalyses' median, the smallest trend is 0.07 ± 0.06 mm decade^{-1} in March and the largest is in August (0.33 ± 0.18 mm decade^{-1}). This seasonal dependency of the IWV trend is in accordance with most recent estimates over the same period by Oshima and Yamazaki (2017), who calculated 0.09 mm decade^{-1} in winter (January–March) and 0.3 mm decade^{-1} in summer (July–September), based on ERAI. Considering the percentage trends, relative to the climatological monthly means, the reanalyses agree that the highest trend (4%–6% decade^{-1}) occurs in the cold season (October–January), while the summer trends account only for 1%–3% decade^{-1}.

In general, the cross-reanalysis differences in the Arctic-averaged IWV trends are minor, except for CFSR being an outlier in summer because of its negative IWV trend over the ice-covered Arctic Ocean [see section 3a(2)]. Figure 8 indicates differences in the trend across the four reanalyses ranging from 0.02 mm decade^{-1} in January to 0.17 mm decade^{-1} in July. However, it is important to emphasize that the spatial averaging smears the considerable cross-reanalysis difference over the central Arctic in the extended summer (May–October), discussed in the previous sections.

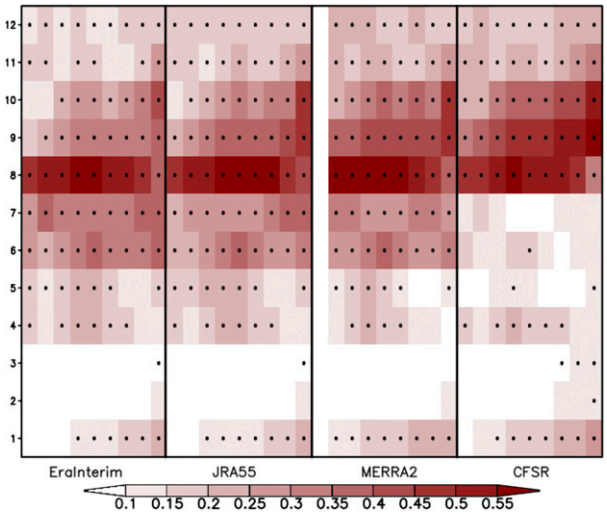

FIG. 9. Monthly IWV trends (mm decade^{-1}) over moving 30-yr periods for the central Arctic (≥70°N) for the four reanalyses (CFSR, ERAI, JRA-55, MERRA2). Nine trends are displayed for each reanalysis. The first 30-yr trend is calculated for the period 1979–2008, the next for 1980–2009, and so on. The *x* axis indicates the nine periods for each individual reanalysis and the *y* axis indicates the 12 months. Stippling indicates significant trends (at the 95% level).

Figure 8 further shows that different reanalyses show the maximum trend in different months. The maximum trend is shifted in CFSR toward the end of the summer, with the absolute maximum occurring in September. In contrast, the other reanalyses show the maximum trend in midsummer (July–August). This is consistent with the monthly and regional differences in IWV trends discussed in section 3a(2), where we found that CFSR has the minimum (maximum) trend out of all reanalyses over the Arctic Ocean in summer (autumn).

The trend calculations for the nine 30-yr moving windows (1979–2008, 1980–2009, etc.) confirm the robustness of the positive trend over the central Arctic across the reanalyses throughout the period (Fig. 9). Further, this figure indicates that the spread between the reanalyses is smaller than the interannual variability. The figure makes us speculate about an increasing trend magnitude, that is, an acceleration of the moistening during the latter part of the period 1979–2016 in autumn (September–October) and in January. Remarkable is the shift of the maximum trend from summer (August) to autumn (September–October) in the most recent 30-yr period (1987–2016), which all reanalyses agree on. This shift is a new, recently emerged phenomenon, and has not been detected in previous studies addressing shorter periods (e.g., until 2010; Serreze et al. 2012). It occurs because of a strong acceleration of the IWV trend over the Barents and Kara Seas in September–October. This becomes apparent if one inspects the associated spatial patterns of the trends for the nine 30-yr moving windows. In September, the IWV trend over the Barents and Kara Seas was negative in the first three periods (1979–2008, 1980–2009, 1981–2010), becomes positive afterward and particularly strengthened in the recent decades (1986–2015, 1987–2016), which we recognize in the positive October trend, too. For example, the comparison of the first period (1979–2008) with the last period (1987–2016) shows an IWV increase of more than 0.8 mm decade^{-1} over that region in autumn, while the changes in August are minor (exemplarily for ERAI shown in Fig. S11). This is associated with changes in the atmospheric circulation in autumn, characterized by a strong SLP increase (up to 5 hPa) over north-central Siberia (Fig. S11), which supports the inflow of warm, humid air from the south into the Barents and Kara Seas. The IWV increase is also related to the sea ice retreat and associated warming observed in that region in autumn, which has been shown to potentially impact the atmospheric circulation pattern in autumn (e.g., Rinke et al. 2013, Cassano and Cassano 2017). The warming signature in the Barents and Kara Seas region shows up also in the ocean since the mid-2000s, associated with the transition to a warm and well-mixed Atlantic-dominated regime (“atlantification”) (Polyakov et al. 2017; Lind et al. 2018). The greater influence of Atlantic-derived waters, such as reduced late autumn–winter sea ice formation, leads to large cold-season temperature anomalies in the lower troposphere, presumably allied with positive anomalies in IWV.

A complementary view of the central Arctic IWV variability by month and year is given by the Hovmöller plots in Fig. S12. Those support the close agreement among the reanalyses and their consistent description of interannual variability, with generally negative anomalies until about the year 2000 and positive anomalies afterward. The latter are highest in summer (June–September). Again, we recognize the shift of the maximum positive anomaly from summer toward autumn (September–October) in the most recent years.

We further examine the IWV trends over the central Arctic with different time windows, exemplarily based on ERAI. For this, we follow the method presented in Dufour et al. (2016). Figure 10 clearly highlights on the one hand the pronounced interannual variability of IWV. Previous studies have shown that this is related to surface air temperature changes (Oshima and Yamazaki 2017), but also reflects atmospheric circulation changes and related airmass transport (e.g., Groves and Francis 2002). Otherwise, the figure demonstrates the general robustness of the recent positive IWV trend. The dominant positive trends in summer, which have occurred

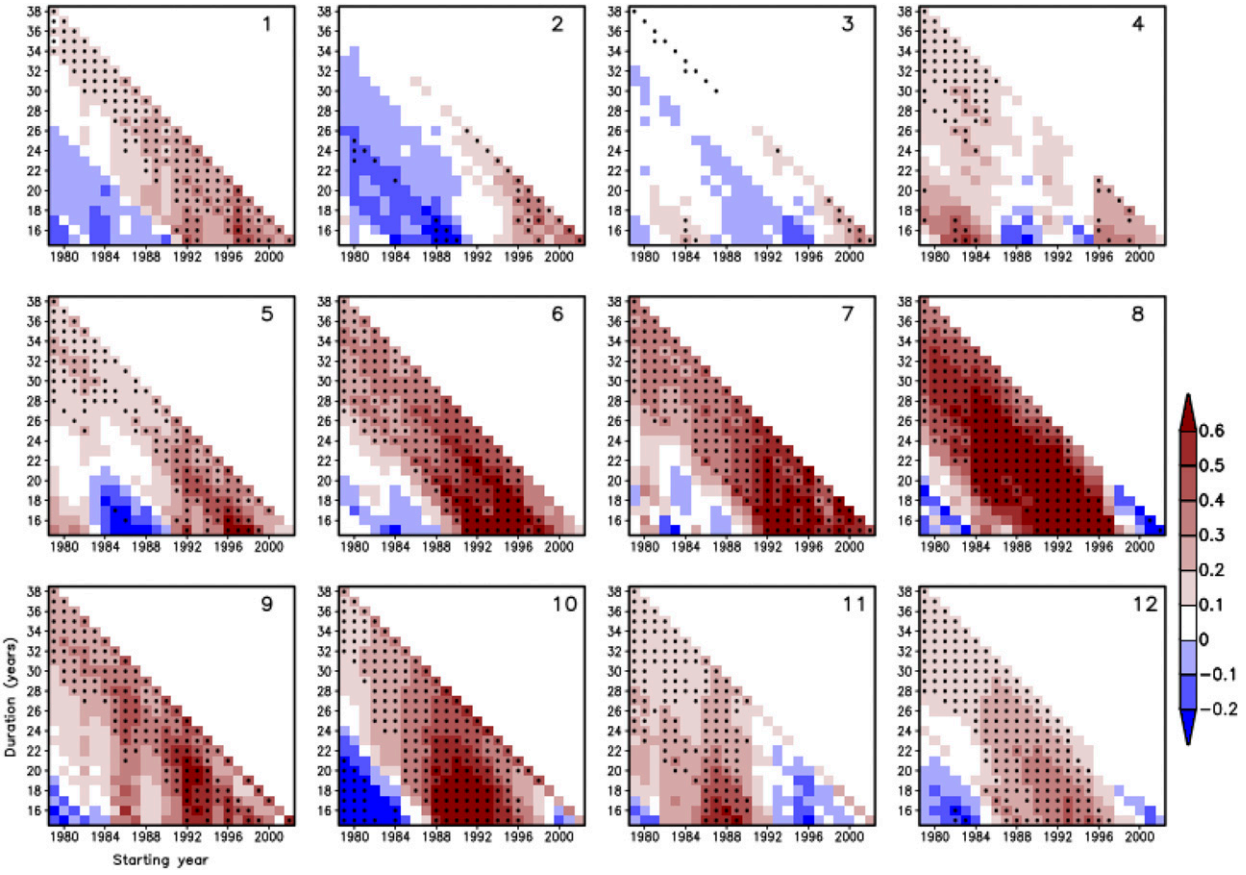

FIG. 10. Monthly IWV trends (mm decade^{-1}) for the central Arctic (≥70°N) for ERAI for different time windows. The trend is calculated for different starting years (x axis) and for different period lengths (years; y axis). Stippling indicates significant trends (at the 95% level).

since the beginning of the 1990s, suggest that the moistening trend in summer is more robust compared to the other seasons.

4. Comparison of IWV trends from reanalyses with observations

The IWV trends from the reanalyses are compared with the circum-Arctic radiosonde data from IGRA for seven Arctic subregions and the Arctic as a whole (Fig. 2). Generally, the reanalyses exhibit a remarkable agreement with the radiosondes (Fig. 11), which is as expected because radiosonde data were assimilated into the reanalyses. The magnitude of differences between individual reanalyses and IGRA data are of the same order as the magnitude of differences among the reanalyses, indicating the relative importance of the assimilated radiosonde dataset for each individual reanalysis, respectively. Importantly, the figure also clearly demonstrates the large uncertainty in the calculated trend, indicated by the 95% confidence interval.

Averaged over all Arctic sites (north of 65°N), consistent positive IWV trends appear in the extended summer (May–October) and negative trends appear in late winter (February–March). We find interesting region-specific annual characteristics in the trends, which are consistent across the datasets (Fig. 11) and support the findings presented in section 3a.

Over the Nordic and Barents Seas, all data show a consistent positive trend in autumn (September–October) and in January. In all other months, most of the trends are not statistically different from zero. We recognize an annual characteristic with maximum (positive trend) in late summer and minimum (small trend of uncertain sign) in late winter. Furthermore, the figure confirms that only CFSR and MERRA2 show significant and large positive trends in summer [discussed in section 3a(2)]. This seems not to be supported by the station data, although it is hard to conclude because of the lack of significance of the observed trend.

In northern Europe, all data agree on a positive trend during most of the year, specifically in spring

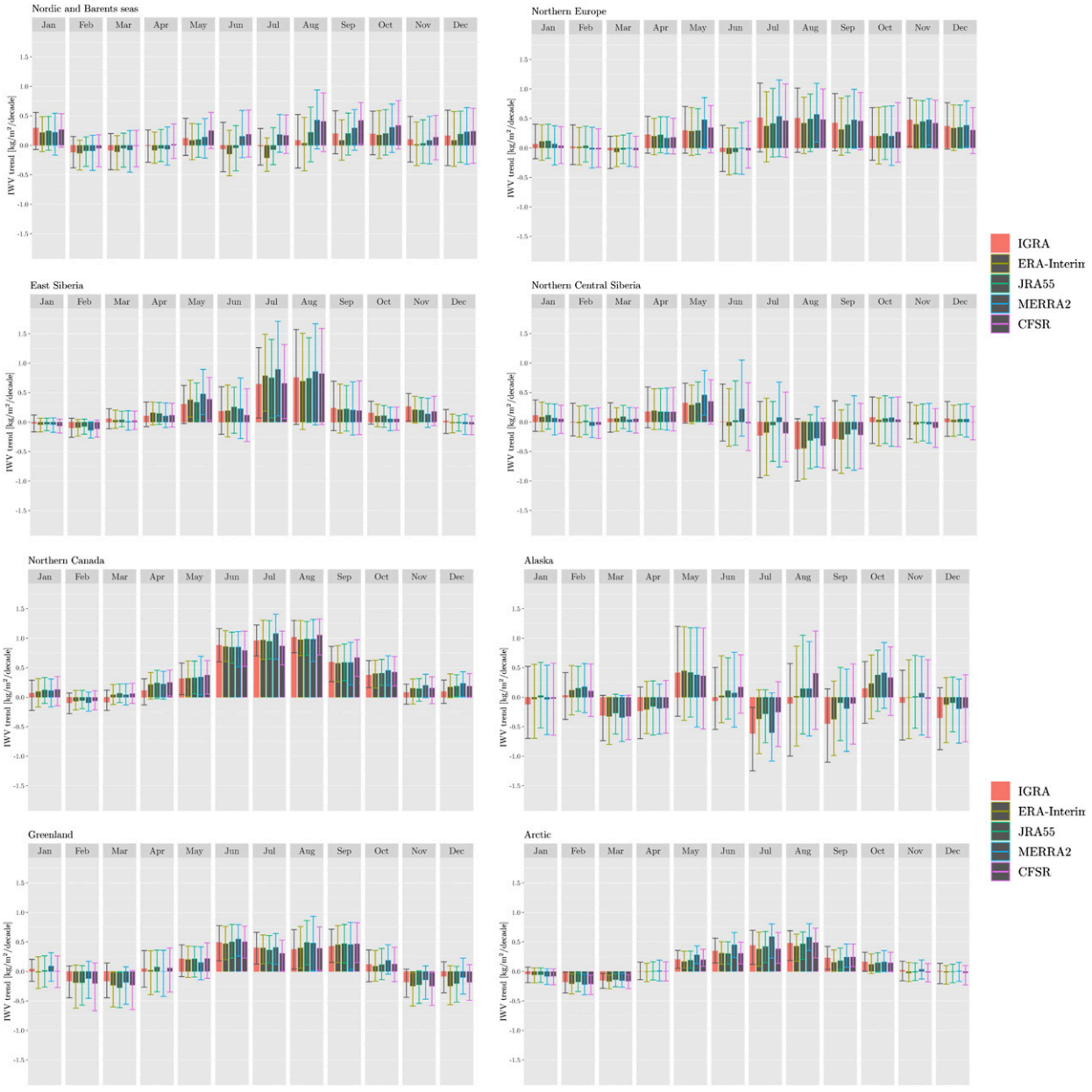

FIG. 11. Monthly IWV trends (mm decade^{-1}) for seven Arctic subregions and for the whole Arctic for 1979–2016. The IGRA station data are shown as red bars and the four reanalyses data are shown as other colored bars (CFSR: pink; ERAI: brown; JRA-55: green; MERRA2: blue). The sampling is the same for all data. The vertical lines indicate the uncertainty with a 95% confidence interval.

(April–May), summer (July–September), and early winter (November–December). Over Greenland, we find positive IWV trends in summer (June–September) and negative trends in winter (November–December, February–March) consistently in all datasets.

Further, Fig. 11 confirms our finding (Fig. 4) that the annual characteristic of the IWV trend in Siberia shows a large spatial variation. This is consistent in all datasets. The IWV in north-central Siberia shows a positive trend in spring (April–May) and a negative trend in summer (particularly in August), associated with circulation changes [section 3a(1)]. By contrast, in east Siberia, the IWV trend is positive during most of the year, with the largest moistening in summer (July–August). Previous studies, which analyzed only the single Siberian station Tiksi (Serreze et al. 2012) could not discuss such important regional differences across Siberia. Further, the figure confirms the exceeding positive

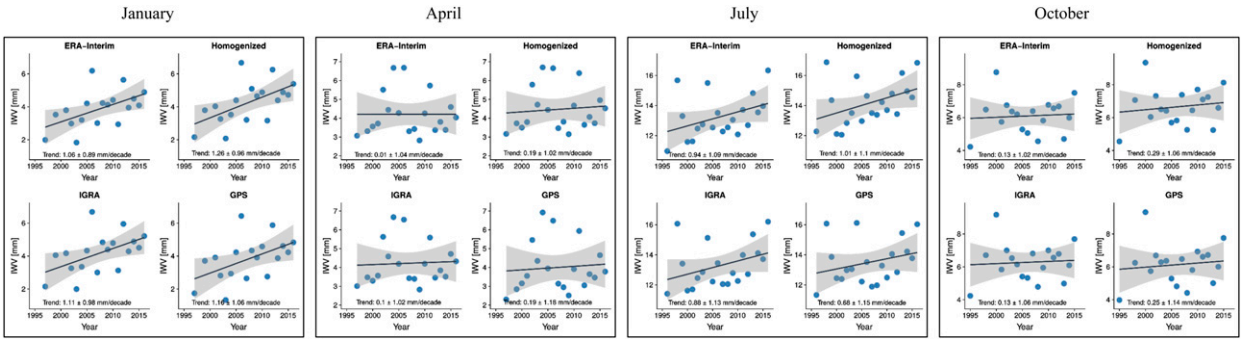

FIG. 12. Monthly IWV (mm) time series at the Ny-Ålesund station for 1994–2016 for the center month of each of the four seasons (January, April, July, October) from ERAI and from IGRA, GPS, and GRUAN-homogenized NYA station observations. The sampling is the same for all data. The gray shading indicates the 95% confidence band for the slope estimator. In each panel, the IWV change is given as linear regression plus and minus two standard deviations. The plots for the remaining months are shown in Fig. S13.

trend in MERRA2 over northern central Siberia in June [discussed in section 3a(2)]. Such a strong moistening is not seen in the station data, but the trend in the observations is anyway insignificant.

In northern Canada, the datasets agree on a positive IWV trend almost throughout the year. Our results based on six stations support the finding of Serreze et al. (2012) who analyzed the three stations Alert, Eureka, and Resolute Bay representing the northern Canadian archipelago, and reported on the strongest observed positive trends in summer and small insignificant trends in winter.

Alaska appears as the region with IWV trends of high uncertainty in all months; the trend does not show a clear seasonal pattern. Our results based on two stations (Barrow and Kotzebue, Alaska) are in contradiction with the findings of Serreze et al. (2012) regarding Barrow during a shorter period (1979–2010). They reported on significant positive IWV trends for this station in summer. The nonconforming results indicate that the calculated trend highly depends on the sampling, because this region is characterized by a strong regional climate variability (Cassano et al. 2011; Bieniek et al. 2014), and the applied period matters too.

Finally, we use the multiple datasets available at Ny-Ålesund to compare them and check the data consistency. Specifically, we look at the monthly IWV changes from station observations of IGRA, homogenized NYA, GPS, and ERAI data for the overlapping period 1994–2016 (Fig. 12, Fig. S13). Importantly, the figures emphasize the large uncertainty of the calculated IWV changes per decade (indicated by the 95% confidence interval) due to the pronounced interannual variability and the relatively short period of 23 years. Nonetheless, the consistency of the results from all data is striking. The IWV changes in the data from IGRA, NYA, and ERAI are shown being consistent with the independent GPS observations.

5. Summary and conclusions

We looked into the question whether a consistent moistening trend all over the Arctic is supported by atmospheric reanalyses and station data. For this, we analyzed the integrated water vapor (IWV) from four reanalyses (CFSR, ERAI, JRA-55, and MERRA2) and radiosonde data from 36 Arctic stations over the period 1979–2016.

In view of polar cap averaging (≥70°N), we confirmed a robust moistening trend in all months based on the reanalyses. The absolute trend is largest in summer and lowest in winter, but has a reverse behavior in the relative magnitudes. We reported on the pronounced interannual variability of the central Arctic IWV trend and showed that the cross-reanalysis spread of the trend is smaller than its variability. Furthermore, we found a recently emerged phenomenon, namely, a shift of the maximum trend from summer to autumn in recent decades, which we related to an accelerated IWV trend over the Barents and Kara Seas in autumn.

The monthly spatial patterns of the IWV trends also suggested that the Arctic has become wetter in almost all regions, but we could not conclude this because most trends were not statistically different from zero. We found significant trends only over specific regions and in specific months. Consistently in all reanalyses, we reported on positive IWV trends over the Atlantic sector of the Arctic in most months, over the Canadian archipelago and Baffin Bay in summer, over parts of the Siberian Arctic sector (Chukchi and East Siberian Seas in autumn, northern Laptev Sea in spring, and east Siberia in summer), and over the central Arctic Ocean in autumn and winter. Negative IWV trends consistently occur over

eastern Siberia and the Bering Strait region in winter and over north-central Siberia in summer. We provided an estimate of the ''typical'' (median of the four reanalyses) regional IWV trend patterns for each month.

Although the reanalyses agree on the spatiotemporal IWV trend patterns, they substantially disagree on the regional trend magnitudes. We identified the summer and the Arctic portion of the North Atlantic (Nordic and Barents Seas), the central Arctic Ocean and north-central Siberia as the season and the regions of greatest absolute differences among the reanalyses. For that, we nominated CFSR and MERRA2 as the outliers, compared to the reanalyses median. Therefore, out of the examined four reanalyses, we recommend to rather use JRA-55 (which is closest to the median trend) or ERAI for IWV trend studies. Furthermore, the ECMWF successor reanalysis, ERA5, should be inspected, as ERA5 provides more information on which individual observations have passed quality control and were assimilated.

It is difficult to identify the detailed causes for the presented differences in reanalyses IWV trends. Basically, these are changes in atmospheric circulation (linked to moisture transport), air temperature (linked to the vapor carrying capacity of the air), and SST and sea ice cover (both linked to vertical moisture and heat fluxes into the atmosphere), which all cause IWV changes. We discussed that the cross-reanalysis differences in the SLP trend can lead to regional differences in moisture transport. Associated with this, we showed (exemplarily for ERAI) that the patterns of the trends in IWV and net moisture transport match well, which indicates that differences in moisture transport play a key role for the IWV trend differences. Furthermore, we presented mostly sea ice–driven cross-reanalysis differences in the evaporation trend, particularly in the cold season when large air–ocean temperature differences occur, which contribute to the reported IWV trend differences.

Furthermore, differences in the selection and weighting of data for assimilation into the reanalyses can contribute to cross-reanalysis differences in IWV trends. As all reanalyses assimilate the radiosonde data available, the differences should arise mainly from model physics or satellite data assimilation, for example, the choice of satellite instruments, calibration technique, and forward operators. Further, particularly in the data-sparse central Arctic Ocean (>80°N) where hardly any satellite data are assimilated over sea ice, the models behind the reanalyses (and their different physics and dynamics) play an important role. Specifically, the different description of moist processes can lead to differences in IWV among the reanalyses. For instance, the models use different parameterizations for deep and shallow convection, and convective and nonconvective clouds, which affects the atmospheric water budget.

The comparison with station observations supported the presented reanalysis-based results. We showed that the long-term IWV trends from the reanalyses exhibit a remarkable agreement with the radiosonde data from 36 Arctic stations in terms of spatiotemporal patterns. The analysis for seven subregions confirmed the region-specific annual characteristics in the trends consistently across the datasets. Unfortunately, the station data could not ultimately confirm the outliers identified for the largest cross-reanalysis differences in the Nordic and Barents Seas and north-central Siberia in summer because of the lack of significance of the observed trends.

In addition, the scarce and nonuniform distribution of stations can provide misleading conclusions. For example, the all-station-averaged (Arctic) negative trend derived for February/March disappears in the reanalyses, which show a moistening when the full central Arctic (≥70°N) is considered. This emphasizes the strong need for long-term observations in the remote Arctic regions to be able to finally reason about the derived IWV trends there. For this, upcoming satellite missions could help.

Finally, we compared the reanalysis (exemplarily ERAI) and the multiple datasets (IGRA and GRUAN radiosonde data, GPS data) that are available at Ny-Ålesund for the overlapping period 1994–2016. We demonstrated the overall data consistency, which qualifies them all for interpreting IWV changes.

Acknowledgments. We gratefully acknowledge the funding by the Deutsche Forschungsgemeinschaft (DFG, German Research Foundation)—Project 268020496—TRR 172, within the Transregional Collaborative Research Center ''Arctic Amplification: Climate Relevant Atmospheric and Surface Processes, and Feedback Mechanisms (AC)^3.'' The study was also supported by the Academy of Finland via projects Today (Contract 308441) and AFEC (Contract 317999). This work is a contribution to the project INTAROS, which has received funding from the European Union's Horizon 2020 research and innovation program under Grant Agreement 727890. We thank Ines Hebestadt for help with the figures. Finally, we thank three anonymous reviewers for their valuable comments on this manuscript.

REFERENCES

Alshawaf, F., F. Zus, K. Balidakis, Z. Deng, M. Hoseini, G. Dick, and J. Wickert, 2018: On the statistical significance of climatic trends estimated from GPS tropospheric time series. *J. Geophys. Res. Atmos.*, **123**, 10 967–10 990, https://doi.org/10.1029/2018JD028703.

AMAP, 2017: Snow, Water, Ice and Permafrost in the Arctic (SWIPA) 2017. Arctic Monitoring and Assessment Programme (AMAP), Oslo, Norway, 269 pp.

Bevis, M., S. Businger, T. Herring, C. Rocken, R. Anthes, and R. Wave, 1992: GPS meteorology: Remote sensing of atmospheric water vapor using the global positioning system. *J. Geophys. Res.*, **97**, 15 787–15 801, https://doi.org/10.1029/92JD01517.

Bieniek, P. A., J. E. Walsh, R. L. Thoman, and U. S. Bhatt, 2014: Using climate divisions to analyze variations and trends in Alaska temperature and precipitation. *J. Climate*, **27**, 2800–2818, https://doi.org/10.1175/JCLI-D-13-00342.1.

Bintanja, R., and F. M. Selten, 2014: Future increases in Arctic precipitation linked to local evaporation and sea ice retreat. *Nature*, **509**, 479–482, https://doi.org/10.1038/nature13259.

Bodeker, G. E., and Coauthors, 2016: Reference upper-air observations for climate: From concept to reality. *Bull. Amer. Meteor. Soc.*, **97**, 123–135, https://doi.org/10.1175/BAMS-D-14-00072.1.

Boisvert, L. N., D. L. Wu, and C.-L. Shie, 2015: Increasing evaporation amounts seen in the Arctic between 2003 and 2013 from AIRS data. *J. Geophys. Res. Atmos.*, **120**, 6865–6881, https://doi.org/10.1002/2015JD023258.

——, M. A. Webster, A. A. Petty, T. Markus, D. H. Bromwich, and R. I. Cullather, 2018: Intercomparison of precipitation estimates over the Arctic Ocean and its peripheral seas from reanalyses. *J. Climate*, **31**, 8441–8462, https://doi.org/10.1175/JCLI-D-18-0125.1.

Cassano, E. N., and J. J. Cassano, 2017: Atmospheric response to anomalous autumn surface forcing in the Arctic basin. *J. Geophys. Res. Atmos.*, **122**, 9011–9023, https://doi.org/10.1002/2017JD026765.

——, ——, and M. Nolan, 2011: Synoptic weather pattern controls on temperature in Alaska. *J. Geophys. Res.*, **116**, D11108, https://doi.org/10.1029/2010JD015341.

Chung, C. E., H. Cha, T. Vihma, P. Räisänen, and D. Decremer, 2013: On the possibilities to use atmospheric reanalyses to evaluate the warming structure in the Arctic. *Atmos. Chem. Phys.*, **13**, 11 209–11 219, https://doi.org/10.5194/acp-13-11209-2013.

Cullather, R. I., and M. G. Bosilovich, 2011: The moisture budget of the polar atmosphere in MERRA. *J. Climate*, **24**, 2861–2879, https://doi.org/10.1175/2010JCLI4090.1.

——, D. H. Bromwich, and M. C. Serreze, 2000: The atmospheric hydrologic cycle over the Arctic Basin from reanalyses. Part I: Comparison with observations and previous studies. *J. Climate*, **13**, 923–937, https://doi.org/10.1175/1520-0442(2000)013<0923:TAHCOT>2.0.CO;2.

Dee, D. P., and Coauthors, 2011: The ERA-Interim reanalysis: Configuration and performance of the data assimilation system. *Quart. J. Roy. Meteor. Soc.*, **137**, 553–597, https://doi.org/10.1002/qj.828.

Deng, Z., G. Gendt, and T. Schöne, 2016: Status of the TIGA Tide Gauge Data Reprocessing at GFZ. *IAG 150 Years, Proceedings of the IAG Scientific Assembly in Potsdam, Germany*, C. Rizos and P. Willis, Eds., Springer International Publishing, 33–40, https://doi.org/10.1007/1345_2015_156.

Dirksen, R. J., M. Sommer, F. J. Immler, D. F. Hurst, R. Kivi, and H. Vömel, 2014: Reference quality upper-air measurements: GRUAN data processing for the Vaisala RS92 radiosonde. *Atmos. Meas. Tech.*, **7**, 4463–4490, https://doi.org/10.5194/amt-7-4463-2014.

Dufour, A., O. Zolina, and S. K. Gulev, 2016: Atmospheric moisture transport to the Arctic: Assessment of reanalyses and analysis of transport components. *J. Climate*, **29**, 5061–5081, https://doi.org/10.1175/JCLI-D-15-0559.1.

Durre, I., R. S. Vose, and D. B. Wuertz, 2006: Overview of the integrated global radiosonde archive. *J. Climate*, **19**, 53–68, https://doi.org/10.1175/JCLI3594.1.

Elliott, W. P., and D. J. Gaffen, 1991: On the utility of radiosonde humidity archives for climate studies. *Bull. Amer. Meteor. Soc.*, **72**, 1507–1520, https://doi.org/10.1175/1520-0477(1991)072<1507:OTUORH>2.0.CO;2.

Francis, J. A., D. M. White, J. J. Cassano, W. J. Gutowski, L. D. Hinzman, M. M. Holland, M. A. Steele, and C. J. Vorosmarty, 2009: An Arctic hydrologic system in transition: Feedbacks and impacts on terrestrial, marine, and human life. *J. Geophys. Res.*, **114**, G04019, https://doi.org/10.1029/2008JG000902.

Fujiwara, M., and Coauthors, 2017: Introduction to the SPARC Reanalysis Intercomparison Project (S-RIP) and overview of the reanalysis systems. *Atmos. Chem. Phys.*, **17**, 1417–1452, https://doi.org/10.5194/acp-17-1417-2017.

Gelaro, R., and Coauthors, 2017: The Modern-Era Retrospective Analysis for Research and Applications, version 2 (MERRA-2). *J. Climate*, **30**, 5419–5454, https://doi.org/10.1175/JCLI-D-16-0758.1.

Ghatak, D., and J. Miller, 2013: Implications for Arctic amplification of changes in the strength of the water vapor feedback. *J. Geophys. Res. Atmos.*, **118**, 7569–7578, https://doi.org/10.1002/jgrd.50578.

Gimeno-Sotelo, L., R. Nieto, M. Vázquez, and L. Gimeno, 2018: A new pattern of the moisture transport for precipitation related to the Arctic sea ice extent drastic decline. *Earth Syst. Dyn.*, **9**, 611–625, https://doi.org/10.5194/esd-9-611-2018.

Groves, D. G., and J. A. Francis, 2002: Variability of the Arctic atmospheric moisture budget from TOVS satellite data. *J. Geophys. Res.*, **107**, 4785, https://doi.org/10.1029/2002JD002285.

IPCC, 2013: *Climate Change 2013: The Physical Science Basis*. Cambridge University Press, 1535 pp., https://doi.org/10.1017/CBO9781107415324.

Jakobson, E., and T. Vihma, 2010: Atmospheric moisture budget over the Arctic on the basis of the ERA-40 reanalysis. *Int. J. Climatol.*, **30**, 2175–2194, https://doi.org/10.1002/joc.2039.

Kiktev, D., D. M. H. Sexton, L. Alexander, and C. K. Folland, 2003: Comparison of modelled and observed trends in indices of daily climate extremes. *J. Climate*, **16**, 3560–3571, https://doi.org/10.1175/1520-0442(2003)016<3560:COMAOT>2.0.CO;2.

Kobayashi, S., and Coauthors, 2015: The JRA-55 Reanalysis: General specifications and basic characteristics. *J. Meteor. Soc. Japan. Ser. II*, **93**, 5–48, https://doi.org/10.2151/JMSJ.2015-001.

Komatsu, K. K., V. A. Alexeev, I. A. Repina, and Y. Tachibana, 2018: Poleward upgliding Siberian atmospheric rivers over sea ice heat up Arctic upper air. *Sci. Rep.*, **8**, https://doi.org/10.1038/S41598-018-21159-6.

Kopec, B. G., X. Feng, F. A. Michel, and E. S. Posmentier, 2016: Influence of sea ice on Arctic precipitation. *Proc. Natl. Acad. Sci. USA*, **113**, 46–51, https://doi.org/10.1073/pnas.1504633113.

Lewis, E. L., E. P. Jones, P. Lemke, T. D. Prowse, and P. Wadhams, Eds., 2000: *The Freshwater Budget of the Arctic Ocean*. Nato Science Series: II, Vol. 70, Kluwer, 623 pp.

Lind, S., R. B. Ingvaldsen, and T. Furevik, 2018: Arctic warming hotspot in the northern Barents Sea linked to declining sea-ice import. *Nat. Climate Change*, **8**, 634–639, https://doi.org/10.1038/s41558-018-0205-y.

Lindsay, R., M. Wensnahan, A. Schweiger, and J. Zhang, 2014: Evaluation of seven different atmospheric reanalysis products

in the Arctic. *J. Climate*, **27**, 2588–2606, https://doi.org/10.1175/JCLI-D-13-00014.1.

Liu, Y., J. R. Key, J. A. Francis, and X. Wang, 2007: Possible causes of decreasing cloud cover in the Arctic winter, 1982-2000. *J. Geophys. Res.*, **34**, L14705, https://doi.org/10.1029/2007GL030042.

Maturilli, M., and M. Kayser, 2016: Homogenized radiosonde record at station Ny-Ålesund, Spitsbergen, 1993-2014. PANGAEA, accessed 12 November 2018, https://doi.org/10.1594/PANGAEA.845373.

——, and ——, 2017a: Arctic warming, moisture increase and circulation changes observed in the Ny-Ålesund homogenized radiosonde record. *Theor. Appl. Climatol.*, **130**, 1–17, https://doi.org/10.1007/s00704-016-1864-0.

——, and ——, 2017b: Homogenized radiosonde record at station Ny-Ålesund, Spitsbergen, 2015-2016, PANGAEA, accessed 12 November 2018, https://doi.org/10.1594/PANGAEA.875196.

Miloshevich, L. M., H. Vömel, A. Paukkunen, A. J. Heymsfield, and S. J. Oltmans, 2001: Characterization and correction of relative humidity measurements from Vaisala RS80-A radiosondes at cold temperatures. *J. Atmos. Oceanic Technol.*, **18**, 135–156, https://doi.org/10.1175/1520-0426(2001)018<0135:CACORH>2.0.CO;2.

Moradi, I., B. Soden, R. Ferraro, P. Arkin, and H. Vömel, 2013: Assessing the quality of humidity measurements from global operational radiosonde sensors. *J. Geophys. Res. Atmos.*, **118**, 8040–8053, https://doi.org/10.1002/JGRD.50589.

Naakka, T., T. Nygård, and T. Vihma, 2018: Arctic humidity inversions: Climatology and processes. *J. Climate*, **31**, 3765–3787, https://doi.org/10.1175/JCLI-D-17-0497.1.

——, ——, ——, J. Sedlar, and R. Graversen, 2019: Atmospheric moisture transport between mid-latitudes and the Arctic: Regional, seasonal and vertical distributions. *Int. J. Climatol.*, **39**, 2862–2879, https://doi.org/10.1002/JOC.5988.

Ning, T., and Coauthors, 2016b: The uncertainty of the atmospheric integrated water vapour estimated from GNSS observations. *Atmos. Meas. Tech.*, **9**, 79–92, https://doi.org/10.5194/amt-9-79-2016.

——, J. Wickert, Z. Deng, S. Heise, G. Dick, S. Vey, and T. Schöne, 2016a: Homogenized time series of the atmospheric water vapor content obtained from the GNSS reprocessed data. *J. Climate*, **29**, 2443–2456, https://doi.org/10.1175/JCLI-D-15-0158.1.

O'Gorman, P. A., and C. J. Muller, 2010: How closely do changes in surface and column water vapor follow Clausius–Clapeyron scaling in climate change simulations? *Environ. Res. Lett.*, **5**, 025207, https://doi.org/10.1088/1748-9326/5/2/025207.

Oshima, K., and K. Yamazaki, 2017: Atmospheric hydrological cycles in the Arctic and Antarctic during the past four decades. *Czech Polar Rep.*, **7** (2), 169–180, https://doi.org/10.5817/CPR2017-2-17.

Parker, W. S., 2016: Reanalyses and observations: What's the difference? *Bull. Amer. Meteor. Soc.*, **97**, 1565–1572, https://doi.org/10.1175/BAMS-D-14-00226.1.

Polyakov, I. V., and Coauthors, 2017: Greater role for Atlantic inflows on sea-ice loss in the Eurasian Basin of the Arctic. *Ocean Sci.*, **356**, 285–291, https://doi.org/10.1126/SCIENCE.AAI8204.

Rinke, A., C. Melsheimer, K. Dethloff, and G. Heygster, 2009: Arctic total water vapor: Comparison of regional climate simulations with observations, and simulated decadal trends. *J. Hydrometeor.*, **10**, 113–129, https://doi.org/10.1175/2008JHM970.1.

——, K. Dethloff, W. Dorn, D. Handorf, and J. C. Moore, 2013: Simulated Arctic atmospheric feedbacks associated with late summer sea ice anomalies. *J. Geophys. Res. Atmos.*, **118**, 7698–7714, https://doi.org/10.1002/JGRD.50584.

——, M. Maturilli, R. M. Graham, H. Matthes, D. Handorf, L. Cohen, S. R. Hudson, and J. C. Moore, 2017: Extreme cyclone events in the Arctic: Wintertime variability and trends. *Environ. Res. Lett.*, https://doi.org/10.1088/1748-9326/AA7DEF.

Saha, S., and Coauthors, 2010: The NCEP Climate Forecast System Reanalysis. *Bull. Amer. Meteor. Soc.*, **91**, 1015–1058, https://doi.org/10.1175/2010BAMS3001.1.

——, and Coauthors, 2014: The NCEP Climate Forecast System version 2. *J. Climate*, **27**, 2185–2208, https://doi.org/10.1175/JCLI-D-12-00823.1.

Schröder, M., and Coauthors, 2018: The GEWEX Water Vapor Assessment archive of water vapour products from satellite observations and reanalyses. *Earth Syst. Sci. Data*, **10**, 1093–1117, https://doi.org/10.5194/essd-10-1093-2018.

Screen, J., and I. Simmonds, 2010: The central role of diminishing sea ice in recent Arctic temperature amplification. *Nature*, **464**, 1334–1337, https://doi.org/10.1038/NATURE09051.

Seidel, D. J., and Coauthors, 2009: Reference upper-air observations for climate: Rationale, progress, and plans. *Bull. Amer. Meteor. Soc.*, **90**, 361–369, https://doi.org/10.1175/2008BAMS2540.1.

Serreze, M. C., and R. G. Barry, 2011: Processes and impacts of Arctic amplification: A research synthesis. *Global Planet. Change*, **77**, 85–96, https://doi.org/10.1016/j.gloplacha.2011.03.004.

——, ——, and J. E. Walsh, 1995: Atmospheric water vapor characteristics at 70°N. *J. Climate*, **8**, 719–731, https://doi.org/10.1175/1520-0442(1995)008<0719:AWVCA>2.0.CO;2.

——, and Coauthors, 2006: The large-scale freshwater cycle of the Arctic. *J. Geophys. Res.*, **111**, C11010, https://doi.org/10.1029/2005JC003424.

——, A. P. Barrett, and J. J. Cassano, 2011: Circulation and surface controls on the lower tropospheric air temperature field of the Arctic. *J. Geophys. Res.*, **116**, D07104, https://doi.org/10.1029/2010JD015127.

——, ——, and J. Stroeve, 2012: Recent changes in tropospheric water vapor over the Arctic as assessed from radiosondes and atmospheric reanalyses. *J. Geophys. Res.*, **117**, D10104, https://doi.org/10.1029/2011JD017421.

Sherwood, S. C., S. Bony, and J. L. Dufresne, 2014: Spread in model climate sensitivity traced to atmospheric convective mixing. *Nature*, **505**, 37–42, https://doi.org/10.1038/nature12829.

Sommer, M., R. Dirksen, and F. Immler, 2012: RS92 GRUAN Data Product Version 2 (RS92-GDP.2). GRUAN Lead Centre, accessed 15 November 2018, https://doi.org/10.5676/GRUAN/RS92-GDP.2.

Steinke, S., S. Eikenberg, U. Löhnert, G. Dick, D. Klocke, P. Di Girolamo, and S. Crewell, 2015: Assessment of small-scale integrated water vapour variability during HOPE. *Atmos. Chem. Phys.*, **15**, 2675–2692, https://doi.org/10.5194/acp-15-2675-2015.

Stroeve, J. C., M. C. Serreze, J. E. Kay, M. M. Holland, W. N. Meier, and A. P. Barrett, 2012: The Arctic's rapidly shrinking sea ice cover: a research synthesis. *Climatic Change*, **110**, 1005–1027, https://doi.org/10.1007/s10584-011-0101-1.

Thorne, P. W., and R. S. Vose, 2010: Reanalyses suitable for characterizing long-term trends. *Bull. Amer. Meteor. Soc.*, **91**, 353–362, https://doi.org/10.1175/2009BAMS2858.1.

Trenberth, K. E., J. T. Fasullo, and J. Mackaro, 2011: Atmospheric moisture transports from ocean to land and global energy flows in reanalyses. *J. Climate*, **24**, 4907–4924, https://doi.org/10.1175/2011JCLI4171.1.

Vihma, T., and Coauthors, 2016: The atmospheric role in the Arctic water cycle: A review on processes, past and future changes, and their impacts. *J. Geophys. Res. Biogeosci.*, **121**, 586–620, https://doi.org/10.1002/2015JG003132.

Wang, J., L. Zhang, A. Dai, T. V. Hove, and J. V. Baelen, 2007: A near-global: 2-hourly data set of atmospheric precipitable water from ground-based GPS measurement. *J. Geophys. Res.*, **112**, D11107, https://doi.org/10.1029/2006JD007529.

Wendisch, M., and Coauthors, 2017: Understanding causes and effects of rapid warming in the Arctic. *Eos, Trans. Amer. Geophys. Union*, **98**, https://doi.org/10.1029/2017EO064803.

Woods, C., and R. Caballero, 2016: The role of moist intrusions in winter Arctic warming and sea ice decline. *J. Climate*, **29**, 4473–4485, https://doi.org/10.1175/JCLI-D-15-0773.1.

Zahn, M., M. Akperov, A. Rinke, F. Feser, and I. I. Mokhov, 2018: Trends of cyclone characteristics in the Arctic and their patterns from different re-analysis data. *J. Geophys. Res. Atmos.*, **123**, 2737–2751, https://doi.org/10.1002/2017JD027439.

Zhang, X., J. He, J. Zhang, I. Polyakov, R. Gerdes, J. Inoue, and P. Wu, 2012: Enhanced poleward moisture transport and amplified northern high-latitude wetting trend. *Nat. Climate Change*, **3**, 47–5, https://doi.org/10.1038/nclimate1631.